
SINGLE-NEURON DEEP GENERATIVE MODEL UNCOVERS UNDERLYING PHYSICS OF NEURONAL ACTIVITY IN CA IMAGING DATA

Jordi Abante *
Dept. of Biomedical Sciences
Universitat de Barcelona
Barcelona, Spain
jordi.abante@ub.edu

Angelo Piga
Dept. of Condensed Matter Physics
Universitat de Barcelona
Barcelona, Spain

Berta Ros
Dept. of Biomedical Sciences
Universitat de Barcelona
Barcelona, Spain

Clara F López-León
Dept. of Condensed Matter Physics
Universitat de Barcelona
Barcelona, Spain

Josep M Canals
Dept. of Biomedical Sciences
Universitat de Barcelona
Barcelona, Spain

Jordi Soriano
Dept. of Condensed Matter Physics
Universitat de Barcelona
Barcelona, Spain

February 4, 2025

ABSTRACT

Calcium imaging has become a powerful alternative to electrophysiology for studying neuronal activity, offering spatial resolution and the ability to measure large populations of neurons in a minimally invasive manner. This technique has broad applications in neuroscience, neuroengineering, and medicine, enabling researchers to explore the relationship between neuron location and activity. Recent advancements in deep generative models (DGMs) have facilitated the modeling of neuronal population dynamics, uncovering latent representations that provide insights into behavior prediction and neuronal variance. However, these models often rely on spike inference algorithms and primarily focus on population-level dynamics, limiting their applicability for single-neuron analyses. To address this gap, we propose a novel framework for single-neuron representation learning using autoregressive variational autoencoders (AVAEs). Our approach embeds individual neurons' spatiotemporal signals into a reduced-dimensional space without the need for spike inference algorithms. The AVAE excels over traditional linear methods by generating more informative and discriminative latent representations, improving tasks such as visualization, clustering, and the understanding of neuronal activity. Additionally, the reconstruction performance of the AVAE outperforms the state of the art, demonstrating its ability to accurately recover the original fluorescence signal from the learned representation. Using realistic simulations, we show that our model captures underlying physical properties and connectivity patterns, enabling it to distinguish between different firing and connectivity types. These findings position the AVAE as a versatile and powerful tool for advancing single-neuron analysis and lays the groundwork for future integration of multimodal single-cell datasets in neuroscience.

Keywords deep generative models · representation learning · calcium imaging

1 Introduction

Calcium imaging of neuronal activity has emerged as a powerful alternative to electrophysiology, enabling parallel measurement of large neuronal populations in a spatially resolved and minimally invasive manner [1]. In contrast

*Corresponding author.

to electrophysiology, this technique facilitates the study of the interplay between neuron location and activity, e.g., in the context of complex systems [2], neuroengineering [3, 4] and medicine [5, 6, 7]. In addition, the spatial information also allows researchers to determine the observed cell types through other experimental techniques, such as immunohistochemistry (IHC). This broad applicability makes calcium imaging a highly versatile technique that has been used to produce recordings of thousands of neurons [8], to study the activity of sub-cellular structures [9], or to track cells over long periods of time [10].

Calcium imaging data has been extensively used to produce neuronal population models that facilitate the study of the neuronal origin of behavior. Recently, several deep generative models (DGMs) have been proposed to model neuronal population dynamics as a function of behavioral queues [11, 12, 13, 14, 15]. These models attempt to find a latent representation $\mathbf{Z}(t)$ of the population state $\mathbf{X}(t)$, a vector consisting of the observed spikes across the population at time t . These approaches overcome the limitations of previous linear approaches, and result in dimensionality reduction techniques that produce meaningful lower-dimensional neural population dynamics [12, 16]. This work has had a profound impact in neuroscience, providing new powerful approaches for visualization, clustering, or discovery of latent spaces that explain neuronal variance that facilitate the prediction of a future behavior based on past neural activity [15]. These approaches, however, focus on finding useful representations for the population state at a given time. In addition, these approaches rely on *spike inference* algorithms as a pre-processing step [17, 18, 19, 20, 21, 22, 23] and usually also rely on generative models that describe the process through which the observed fluorescence signal arises from the unobserved spike trains (latent variable). Thus, their accuracy depends on the faithfulness of the generative model [20, 23]. Furthermore, these approaches often require arbitrary thresholds that need human supervision during analysis. Recently, discriminative models relying on paired electrophysiological and fluorescence calcium recordings have also been developed, precluding the need for accurate generative models [24]. Nevertheless, these models assume independence across time and require large labeled datasets for every different experimental setting [23].

Finding latent representations of individual neurons, as opposed to the population, offers an alternative representation of the data. Indeed, there have been attempts at finding reduced dimensionality representations of single neurons through linear approaches [6]. Nevertheless, to the best of our knowledge, the potential of representation learning through DGMs to learn useful representations of single neurons has not been explored. Similar to population-level models, this could facilitate common downstream tasks such as visualization, clustering, or even data compression [25], from a single neuron perspective. Additionally, these models provide very fast means to denoise and simulate Ca imaging data, once trained. Lastly, such an approach is instrumental in advancing the multimodal integration of single-cell calcium imaging data with single-cell RNA sequencing (scRNA-seq) data, as well as other modalities.

Here, we propose a new framework for single-neuron representation learning based on variational autoencoders (VAEs) [26]. In particular, we develop an autoregressive VAE (AAVAE) which learns a non-linear mapping that embeds the spatiotemporal signal of individual neurons in a reduced dimensionality space, where one can uncover different subpopulations of neurons and identify activity and connectivity alterations. The proposed approach does not rely on spike inference algorithms, thus simplifying the process. Using biologically-realistic simulated data, we evaluate the reconstruction performance of the algorithm and compare it to the state-of-the-art (SOTA) linear approach, specifically Principal Component Analysis (PCA) showing superior performance. We show that the proposed model implicitly learns the underlying physical model and the connectivity patterns established between neurons. Furthermore, the latent representation found with our AVAE model is better suited for typical subsequent tasks, such as visualization and clustering, compared to SOTA approaches.

2 Methods

2.1 Numerical simulations

To benchmark the proposed approach, we generate realistic simulations that allow us to evaluate the reconstruction accuracy as well as the quality of the learned representation of the proposed approach.

1. A network of connected neurons is constructed, which satisfies the spatial constraints of real neuronal cultures and a realistic mechanism for axonal growth and connectivity [27, 28]. Given this network, the corresponding weighted adjacency matrix \mathbf{W} is defined, with output connection weights randomly sampled from Gaussian distributions with mean $w_E = 6$ and $w_I = -12$ for excitatory and inhibitory neurons, respectively. The inhibitory neurons are randomly selected and encompass 20% of the total population [28].

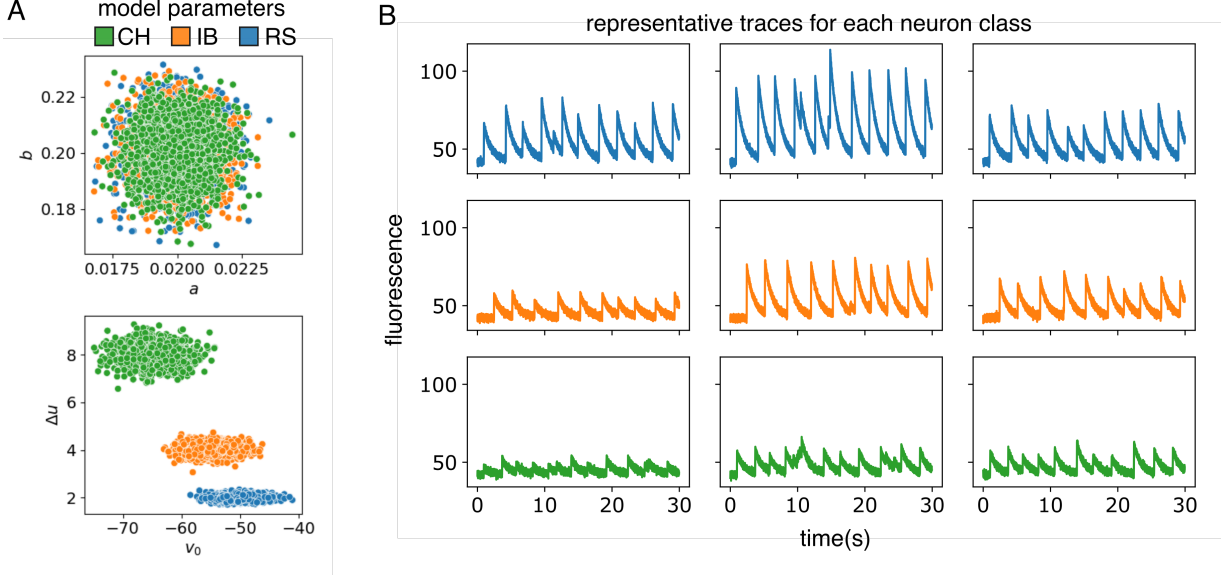


Figure 1: Simulated data. **A.** Parameters a , b , v_0 and Δu for simulated data with each neuron colored according to the corresponding group. Parameters a and b do not result in separation between the groups, whereas v_0 and Δu perfectly separate the three groups. **B.** Four (unnormalized) randomly chosen traces ($\sigma_t = 1$) for each group: RS (blue), IB (orange), and CH (green).

2. The dynamics of each neuron follows Izhikevich’s integrate-and-fire model [29], given by

$$\begin{aligned} \frac{dv}{dt} &= 0.04v^2 + 5v + 140 - u + I + \eta, \\ \frac{du}{dt} &= a(bv - u), \end{aligned} \quad (1)$$

where v is the membrane potential, u a membrane recovery variable, η is a noise term and I is the synaptic input. A neuron ‘spikes’ whenever v reaches a threshold of 30 mV, and the resetting of the neuronal potential after each spike obeys $v \leftarrow v_0$ and $u \leftarrow u + \Delta u$. The parameters a , b , v_0 , and Δu can be adjusted to account for different neuronal firing behaviors [29]. The model is refined by adding pre-synaptic depression dynamics, which accounts for neurotransmitter depletion following repetitive firing [30]. The adjacency matrix \mathbf{W} from point (1) mediates the integration of the several neuronal input currents.

3. The binary spiking temporal series of neurons are converted in fluorescence calcium traces \mathbf{f} using a previous method [20],

$$f_t = F_0 * A(\kappa + p_2(\kappa^2 - \kappa) + p_3(\kappa^3 - \kappa)), \quad t = 1, \dots, T, \quad (2)$$

where F_0 is a fixed baseline, A is a transient amplitude, p_2 and p_3 are fitting parameters, whose values are set to to mimic the genetically encoded calcium indicator (GECI) GCaMP6s [31].

4. To each trace $\mathbf{f} = [f_1, \dots, f_T]^T$ of length T , we add different levels of Gaussian noise $\sigma_t \in \{0.5, 1, 1.5, 2, 2.5\}$, producing the corresponding noisy version \mathbf{x} , allowing us to benchmark the algorithm under different noise conditions. That is,

$$\mathbf{x} = \mathbf{f} + \epsilon, \quad \epsilon \sim \mathcal{N}(0, \sigma_t I_T), \quad (3)$$

where I_T is the $T \times T$ identity matrix.

5. Lastly, before training the AVAE model, the i -th trace from the n -th sample is normalized through the transformation

$$\mathbf{x}_{n,i} = \frac{\mathbf{x}_i - \min_i \mathbf{x}_i}{\max_i \mathbf{x}_i - \min_i \mathbf{x}_i} - 0.5, \quad (4)$$

which provides a scale that is more appropriate for the training of a model. Given the linearity of the transformation, the original scale can be recovered when interested in simulating data in that scale.

We simulate several synthetic cultures, each one containing one type of excitatory neurons, i.e. characterized by the same spiking pattern. Different dynamics are selected by modifying parameters a , b , v_0 , and Δu in Eq. (1). Specifically, we consider the three excitatory cortical cells summarized in Table 1. In particular, the three groups are distinguished by the values of v_0 and Δu , which characterize the resetting part of the model.

Neuron Type	a	b	v_0	Δu
Regular spiking neurons (RS)	0.02	0.2	-65	8
Intrinsically bursting neurons (IB)	0.02	0.2	-55	4
Chattering neurons (CH)	0.02	0.2	-50	2

Table 1: Parameters for different neuron types.

To ensure variability in dynamics across the synthetic cultures, avoiding biases in the simulations, and to test the robustness of our method against noise, we generate five distinct cultures for each type of neuron. These cultures differ in the positions of the cells and the axon connections as defined in point (1). For each neuron, the four parameters of the Izhikevich’s model are allowed to randomly vary around their preset values of Table 1 to consider intrinsic biological variability. As shown in Fig. 1A, parameters v_0 and Δu are the most effective in separating the groups. The dynamics are simulated for a total of 30 s in discrete time steps of 1 ms (Fig. 1B). To remove any potential biases due to the initial phase of the traces and to fully distinguish each culture from one another, we discard the first T_{in}^c steps from the temporal series of each simulated culture, where the superscript c identifies the culture. This length varies from one culture to another to mimic experimental data in which the observer cannot know when the culture is going to activate.

2.2 Experimental data

We consider data obtained from spontaneous activity recordings of mouse primary cortical neurons designed as an *in vitro* tauopathy model. Tauopathies are a group of neurological diseases involving the protein tau, a microtubule-associated protein that, under pathological conditions, becomes hyperphosphorylated and accumulates as ‘tau aggregates’, potentially altering synaptic plasticity and disrupting neuronal network connectivity [32]. Alzheimer’s disease is the most prominent and well-known form of tauopathies [33].

Neurons in culture are grown on glass surfaces as described in [10] and transduced with the GEC1 GCaMP6s. For the experiments, two initially identical sets of cultures are prepared, each 4 mm in diameter and containing about 700 neurons, and termed ‘control’ and ‘tauopathy model’. For the former, neurons are grown following the standard culturing protocol; for the latter, neurons are chronically treated with pathological tau aggregates at day *in vitro* (DIV) 5. Then, both culture sets are cultured identically and their spontaneous activity monitored in parallel along two weeks.

For the results presented here, data is acquired at DIV 12 on a microscope equipped for fluorescence together with a high-speed camera that provides images at 33 Hz and cellular resolution. Spontaneous neuronal activity on both culture sets is recorded for 15 min, and images processed with the software Netcal [34] to extract the fluorescence trace $f_i(t)$ of each neuron i as a function of time. Fluorescence signals are first normalized as $DFf_i(t) \equiv [f_i(t) - f_{i,0}(t)]/f_{i,0}$, where $f_{i,0}$ is the fluorescence signal of neuron i at rest. Then, the signals are further transformed as in Eq. (4) to shape the experimental data to be analyzed.

2.3 Autoregressive Variational Autoencoder

We assume we have N observed calcium traces $\{\mathbf{x}_i\}$ generated by a latent random variable \mathbf{z}_i (Fig. 2A). We allow for each \mathbf{x}_i to depend on \mathbf{z}_i in a complex non-linear way through a neural network with parameters θ . The joint probability can be factorized by using:

$$p(\mathbf{x}, \mathbf{z}) = \prod_{i=1}^N p_{\theta}(\mathbf{x}_i | \mathbf{z}_i) p(\mathbf{z}_i). \tag{5}$$

As customary, we assume $\mathbf{Z}_i \sim \mathcal{N}(0, I)$. Since the posterior distribution $p(\mathbf{z} | \mathbf{x})$ is intractable, we approximate it with the variational approximation $q_{\phi}(\mathbf{z} | \mathbf{x})$ (Fig.2A), which is parametrized by the variational vector of parameters ϕ , defined by a neural network as well. More precisely, we assume $\mathbf{Z} | \mathbf{x} \sim \mathcal{N}(\mu_{\mathbf{z}}(\mathbf{x}), \sigma_{\mathbf{z}}^2(\mathbf{x}))$, where $\mu_{\mathbf{z}}$ and $\log \sigma_{\mathbf{z}}^2$ are the outputs of the neural networks in the encoder (Fig 2B). In addition, given the sequential nature of calcium traces, both the first layer of the encoder and the last layer of the decoder are long short-term memory (LSTM) layers, resulting in an autoregressive model (Fig. 2B). As a result, we have that $\mathbf{X} | \mathbf{z} \sim \mathcal{N}(\mu_{\hat{\mathbf{x}}}(\mathbf{z}), \sigma^2 I)$, where σ^2 is fixed.

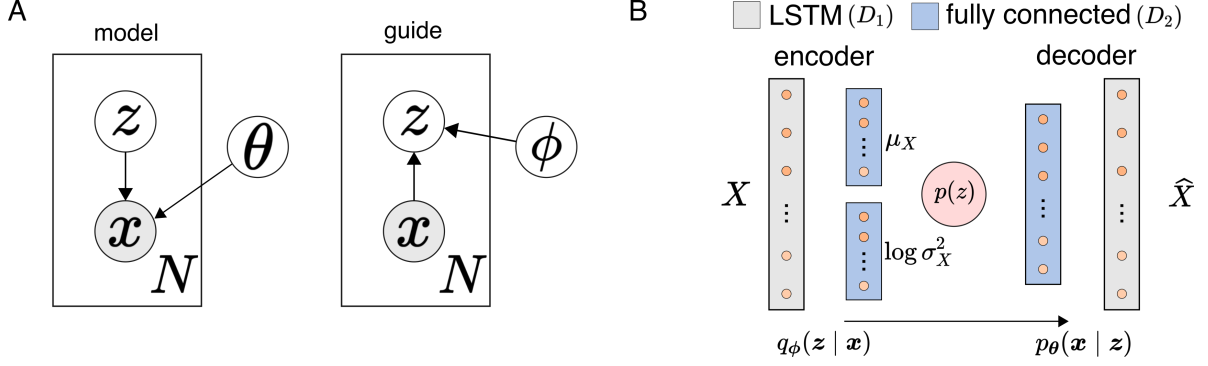


Figure 2: Conceptual representation of the autoregressive variational autoencoder model. **A.** Probabilistic model and variational posterior model in plate notation (shaded circles are observed variables). **B.** Architecture of the implemented autoregressive variational autoencoder (AVAE). The encoder consists of a long short-term memory (LSTM) layer followed by two fully connected linear layers in parallel, encoding the parameters μ_X and $\log \sigma_X^2$ of the variational posterior $q_\phi(\mathbf{z} | \mathbf{x})$. The decoder consists of a fully connected layer followed by an LSTM layer.

Once we have estimated parameters θ and ϕ , we can generate samples of \mathbf{x} by first sampling \mathbf{z} from the prior $p(\mathbf{z})$ and then sampling \mathbf{x} from $p_\theta(\mathbf{x} | \mathbf{z})$.

2.4 Parameter inference

Our goal is to maximize the marginal likelihood

$$p_\theta(\mathbf{x}) = \int p_\theta(\mathbf{x} | \mathbf{z}) p_\theta(\mathbf{z}) d\mathbf{z}. \quad (6)$$

However, this quantity is intractable. As a result, we will seek to optimize a lower bound to the marginal likelihood. For that, we note that we can write the following expression:

$$\begin{aligned} \log p_\theta(\mathbf{x}) &= \mathbb{E}_{q_\phi(\mathbf{z} | \mathbf{x})} [\log p_\theta(\mathbf{x})] \\ &= \mathbb{E}_{q_\phi(\mathbf{z} | \mathbf{x})} \left[\log \left(\frac{p_\theta(\mathbf{x}, \mathbf{z})}{q_\phi(\mathbf{z} | \mathbf{x})} \right) \right] \\ &\quad + \mathbb{E}_{q_\phi(\mathbf{z} | \mathbf{x})} \left[\log \left(\frac{q_\phi(\mathbf{z} | \mathbf{x})}{p_\theta(\mathbf{z} | \mathbf{x})} \right) \right]. \end{aligned} \quad (7)$$

The second term is the Kullback-Leibler (KL) divergence between the variational posterior and the posterior distribution, which is a non-negative quantity. As a result, we have that

$$L_{\theta, \phi}(\mathbf{x}) \equiv \mathbb{E}_{q_\phi(\mathbf{z} | \mathbf{x})} \left[\log \left(\frac{p_\theta(\mathbf{x}, \mathbf{z})}{q_\phi(\mathbf{z} | \mathbf{x})} \right) \right] \leq \log p_\theta(\mathbf{x}). \quad (8)$$

Thus, function $L_{\theta, \phi}(\mathbf{x})$ is usually termed evidence lower bound (ELBO). We can rewrite it as

$$L_{\theta, \phi}(\mathbf{x}) = \mathbb{E}_{q_\phi(\mathbf{z} | \mathbf{x})} [\log p_\theta(\mathbf{x} | \mathbf{z})] - D_{\text{KL}}(q_\phi(\mathbf{z} | \mathbf{x}) \| p_\theta(\mathbf{z})). \quad (9)$$

Thus, the ELBO function consists of a first term which is the expected log-likelihood, plus a second regularization term that ensures that the posterior does not deviate from the prior. More generally, the influence of the KL divergence term can be controlled with a weight β_{KL} , resulting in the loss function of a β -VAE [25], given by

$$\begin{aligned} L_{\theta, \phi}(\mathbf{x}) &= \mathbb{E}_{q_\phi(\mathbf{z} | \mathbf{x})} [\log p_\theta(\mathbf{x} | \mathbf{z})] \\ &\quad - \beta_{\text{KL}} D_{\text{KL}}(q_\phi(\mathbf{z} | \mathbf{x}) \| p_\theta(\mathbf{z})). \end{aligned} \quad (10)$$

The first term can be computed as the Euclidean norm

$$-\log p_\theta(\mathbf{x} | \mathbf{z}) \propto \|\mathbf{x} - d_\theta(\mathbf{z})\|_2^2, \quad (11)$$

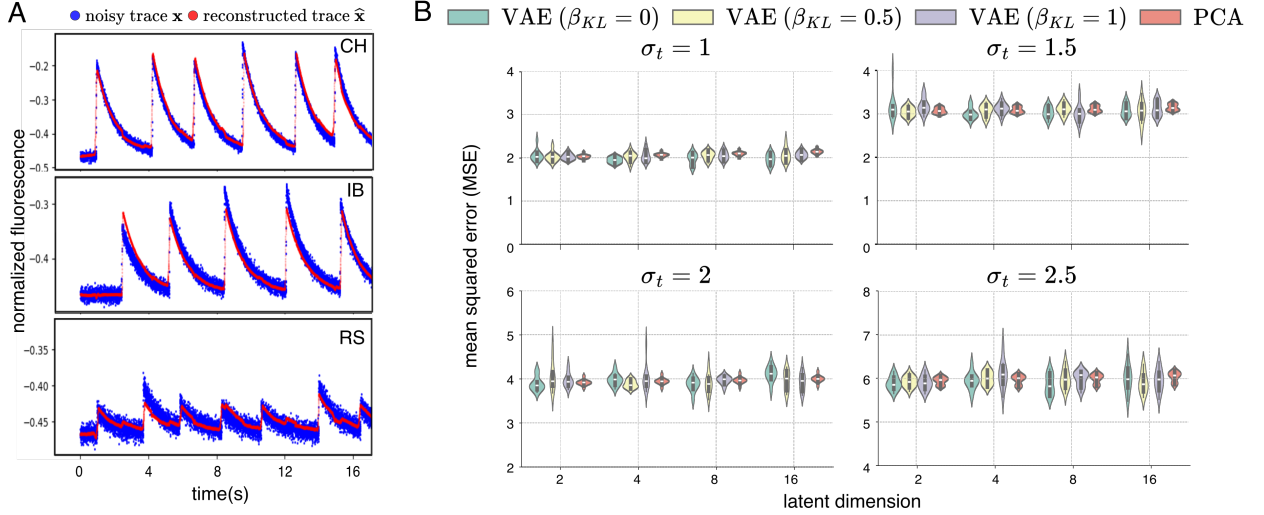


Figure 3: Fluorescence trace reconstruction. **A.** Three representative examples of the noisy trace \mathbf{x} (blue) with $\sigma_t = 1$ and reconstructed $\hat{\mathbf{x}}$ (red) for an AVAE with $D_1 = 128$, $D_2 = 8$, and $\beta_{KL} = 0.5$. **B.** Mean-squared error (MSE) ($\times 10^3$) of the reconstruction for different levels of noise σ_t and latent dimension D_2 (color indicates the corresponding model).

where $d_\theta(\mathbf{z})$ is the output of the decoder, whereas the KL divergence term can be computed analytically since we assume a diagonal Gaussian prior and a diagonal Gaussian posterior. As a result, we have

$$D_{KL}(q||p) = -\frac{1}{2} \sum_{k=1}^K [\log \sigma_k^2 - \sigma_k^2 - \mu_k^2 + 1]. \quad (12)$$

By optimizing Eq. (10) we can find appropriate values for θ and ϕ so that: (i) the log evidence $\log p_\theta(\mathbf{x})$ is large, and (ii) the distribution $q_\phi(\mathbf{z} | \mathbf{x})$ provides a good approximation to the posterior.

2.5 Hyper-parameter optimization

There are two hyper-parameters that we vary regarding the architecture of the AVAE, namely the dimensionality of the first layer D_1 and that of the latent space D_2 . Thus, both for the simulated and real data we trained AVAE models for every pair $(D_1, D_2) = \{(32, 2), (64, 4), (128, 8), (256, 16)\}$. For each pair, we trained an AVAE with a different KL regularization $\beta = 0, 0.5, 1$, to study the effect of this term both regarding reconstruction and latent representation performance. During training we used a learning rate $l_r = 0.005$ with an exponential scheduler with $\gamma = 0.99$. As a result, the learning rate at the k -th epoch η_k was given by $\eta_k = \eta_0 \cdot \gamma^k = 0.005 \cdot 0.99^k$. Finally, we also used early stopping by using a validation dataset with a patience of 5 and $\Delta_{\min} = 0.005$, ensuring that the models would not overfit and generalize to unseen data.

2.6 Reconstruction benchmark

To evaluate the effectiveness in reconstructing the noiseless fluorescence signal \mathbf{f} from the noisy observation \mathbf{x} as constructed in Eq. (3), we compared the proposed approach with PCA by computing the mean-squared error (MSE) between the reconstructed signal and the ground-truth. To ensure a fair comparison between the AVAE and PCA models, we used the first D_2 principal components for PCA as well. The PCA reconstructed signal $\hat{\mathbf{x}}^{PCA}$ is obtained by projecting the data back to the original space using the first D_2 principal components and the corresponding eigenvectors. This process effectively retains the most significant features of the data while minimizing the noise. The reconstruction formula for PCA is given by:

$$\hat{\mathbf{x}}^{PCA} = \mathbf{U}_{D_2} \mathbf{U}_{D_2}^T \mathbf{x} \quad (13)$$

where \mathbf{U}_{D_2} is the matrix of the first D_2 principal components. This formula ensures that the reconstructed signal $\hat{\mathbf{x}}^{PCA}$ captures the primary directions of variance in the data as determined by PCA, thereby providing a denoised version of the input \mathbf{x} .

For each level of noise σ_t , we considered ten different partitions of the data into a training and testing set, which allowed us to study the performance of the models with unseen data. Given the i -th true noiseless fluorescence trace \mathbf{f}_i and the corresponding reconstructed traces, $\hat{\mathbf{x}}_i^{VAE}$ and $\hat{\mathbf{x}}_i^{PCA}$, in the test set of the j -th data partition of the data, the MSE is calculated using:

$$\text{MSE} = \frac{1}{n} \sum_{i=1}^n (\mathbf{f}_i - \hat{\mathbf{x}}_i)^2. \quad (14)$$

This comparison allows us to quantify how well each method recovers the original signal by examining the discrepancies between the original and reconstructed traces. We computed this quantity for the testing set, allowing us to evaluate how well each model generalizes. In each case, we used the same number of latent dimensions for a fair comparison.

2.7 Representation benchmark metrics

To assess the quality of the latent representation learned by the AVAE model in comparison to the PCA embedding within our simulated data, we employed the density-based spatial clustering of applications with noise (DBSCAN) algorithm [35] to cluster neurons in each space. The maximum distance ϵ in the DBSCAN algorithm is a crucial parameter that determines how close points must be to each other to be considered in the same neighborhood. Thus, in each case we optimize this hyperparameter for optimal performance for both $\mathbf{Z}_{D_2}^{VAE}$ and $\mathbf{Z}_{D_2}^{PCA}$, the D_2 -dimensional embeddings obtained via the AVAE model and PCA, respectively. To obtain the PCA embedding using the first D_2 principal components, we used:

$$\mathbf{Z}_{D_2}^{PCA} = \mathbf{X}\mathbf{U}_{D_2}, \quad (15)$$

where \mathbf{X} is the original data matrix with data points as rows and features as columns. \mathbf{U}_{D_2} is the matrix containing the first (D_2) principal component vectors as columns. $\mathbf{Z}_{D_2}^{PCA}$ is the resulting PCA embedding matrix with the transformed data points in the reduced (D_2)-dimensional space.

We evaluated the consistency of the clusters with the original labels using the adjusted Rand index (ARI). For each scenario, we varied the maximum distance parameter ϵ while clustering neurons to find the optimal value based on the ARI in the test set from the j -th data partition, given by

$$\text{ARI} = \frac{\sum_{ij} \binom{n_{ij}}{2} - \left[\sum_i \binom{a_i}{2} \sum_j \binom{b_j}{2} \right] / \binom{n}{2}}{\frac{1}{2} \left[\sum_i \binom{a_i}{2} + \sum_j \binom{b_j}{2} \right] - \left[\sum_i \binom{a_i}{2} \sum_j \binom{b_j}{2} \right] / \binom{n}{2}}, \quad (16)$$

where:

- n is the total number of neurons.
- n_{ij} is the number of neurons in both cluster i of the first clustering and cluster j of the second clustering.
- a_i is the sum of neurons in cluster i of the first clustering.
- b_j is the sum of neurons in cluster j of the second clustering.
- $\binom{x}{2}$ is the binomial coefficient, calculated as $\binom{x}{2} = \frac{x(x-1)}{2}$.

The ARI ranges between -1 and 1, achieving its maximum value when there is perfect agreement between the cluster memberships and the true labels.

3 Results

3.1 Reconstruction benchmark

First, we sought to compare the reconstruction performance of the proposed approach to the SOTA linear approach, i.e., PCA. We generated realistic simulations under different levels of signal-to-noise ratio (SNR) to study the impact that the AVAE architecture and the KL regularization coefficient β_{KL} have, and to compare the performance of the model to a PCA model with the corresponding number of principal components (Fig. 3). We found that the AVAE model

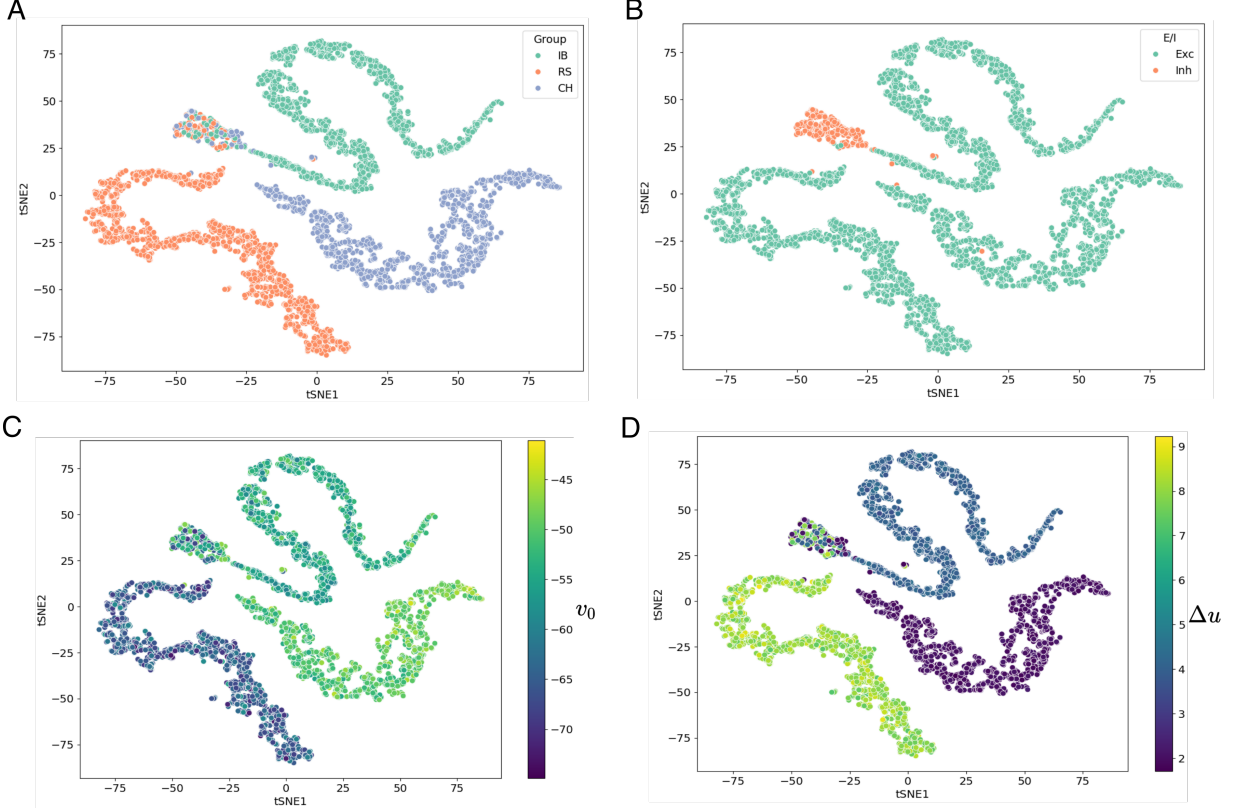


Figure 4: t-SNE of learned representation colored according to neuron firing type (A), connectivity (B), parameter v_0 (C), and parameter Δu (D). Neurons are grouped according to connectivity and firing type, largely driven by parameters v_0 and Δu .

successfully reconstructs the fluorescence signal of unseen data for different types of dynamics (Fig. 3A). Importantly, the AVAE model is able to properly reconstruct the original signal regardless of the phase shift T_{in}^c , suggesting it is learning the underlying physics behind the firings (Fig. 3B). As expected, we found that the performance of all the models deteriorated as the Gaussian noise σ_t added to the fluorescence signal increased. Although the median difference between the models was not generally large, we found that the AVAE model consistently outperforms the PCA model when considering the model with the lowest MSE in the test set, suggesting that the former generalizes better to unseen data, regardless of the regularization coefficient β_{KL} .

3.2 Quality of learned representation in simulated data

When embedding the latent representation \mathbf{Z} using t-distributed stochastic neighbor embedding (t-SNE) [36], we found that neurons grouped according to their dynamical behavior class (CH, IB, RS) regardless of the phase shift T_{in}^c (Fig. 4A). In addition, inhibitory neurons also grouped together, suggesting that the representation is capable of recognizing differences in connectivity in addition to firing dynamics (Fig. 4B).

In order to benchmark the learned representation, we compared that of the AVAE model to the representation learned through PCA by clustering the neurons in the latent space using DBSCAN (Fig. 5A). We observed that the quality of the representation of the test data generally improved for larger values of β_{KL} for the AVAE model, with the median ARI generally increasing with this parameter, consistent with the expected behavior. In addition, we did not observe a decrease in performance when varying the latent dimension D_2 . This is in contrast to PCA, which consistently worsens in performance as D_2 increases. Lastly, we observed that the AVAE model consistently outperformed PCA, in some cases resulting in ARI differences larger of 0.2 for the best performing AVAE model.

Interestingly, the representation learned was highly influenced by the underlying parameters of the dynamical model (Fig. 4C-D). This can also be seen in Fig. 5B, where the informative parameters v_0 and Δu strongly correlate in an antagonistic way with the first seven latent components.

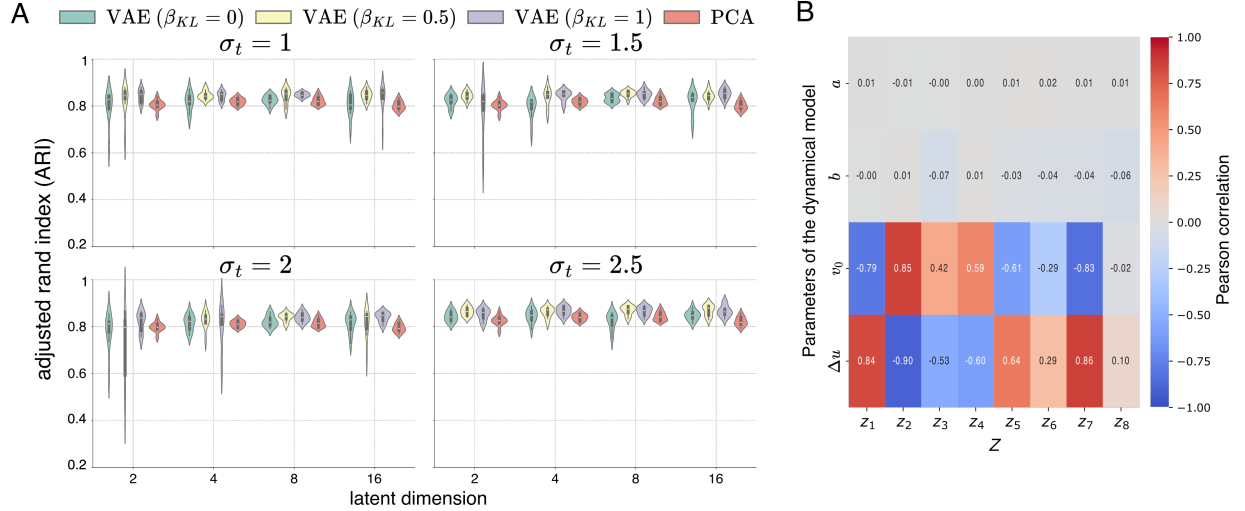


Figure 5: Quality of latent representation in simulated data. **A**. Adjusted Rand index (ARI) of the DBSCAN clustering under different levels of noise σ_t and latent dimension D_2 (color indicates the corresponding model). **B**. Correlation between the parameters of the dynamical model and the latent representation. Parameters a and b do not correlate with any coordinate, whereas the informative parameters v_0 and Δu correlate in an antagonistic way with the first seven coordinates of z .

3.3 Analysis of experimental tauopathy data

When analyzing the *in vitro* recordings that model a tauopathy disease, we also trained several AVAE models and found that a hidden dimensionality of $D_1 = 128$ and a latent space of $D_2 = 8$ dimensions achieved a good compromise between reconstruction and KL divergence error (Fig. 6A), suggesting that the intrinsic dimensionality of the data is well below the original 30k dimensions (i.e., time-points). Consistent with the observations from our simulated data, the reconstruction resulted in a denoised version of the original signal. In addition, the t-SNE projection of the latent space clearly separates the two conditions at hand (Fig. 6B), showing that the latent space offers a valuable representation of the experimental data as well.

4 Discussion

Here, we introduce a novel representation learning algorithm for single neurons using Ca imaging data, built on autoregressive variational autoencoders (AVAE). Through realistic simulations, we demonstrate that our method excels in denoising input signals across various signal-to-noise ratios (SNRs), consistently outperforming PCA. Moreover, our approach generates superior latent representations, irrespective of the SNR, which facilitate further tasks like clustering and visualization. A key advantage of the AVAE is the smoothness of its latent space, imposed by the prior, which results in robust representations that allow for meaningful interpolation between data points—a capability that PCA lacks. Additionally, being a generative model, the AVAE offers flexibility not available in PCA, such as extending into a conditional framework for advanced modeling. We attribute the superior performance of AVAE over PCA to the inductive bias introduced through the LSTM layers, which are specifically designed for temporal data, enhancing its efficacy in handling time-based sequences inherent in neuronal activity recordings.

Our method is notably resilient to phase shifts between biological replicates and generalizes well to unseen data from the same distribution. This robustness stems from the algorithm’s ability to learn the fundamental physical properties governing neuronal spiking, as well as variations in connectivity. When applied to real, *in vitro* data, our method offers good denoising performance even with a relatively simple architecture. The latent representation effectively distinguishes between two conditions and reveals greater heterogeneity in diseased neurons, which can be interpreted as a signature of altered connectivity in the diseased network, resulting in less coordinated neuronal activity consistent with previous results [37]. Thus, our approach not only enhances the accuracy of neuronal data analysis but also provides insights into the underlying biological mechanisms.

Overall, the AVAE shows significant promise not only as an alternative tool for analyzing Ca imaging data but also as a foundational step toward more comprehensive models of neuronal activity. In contrast to previous population DGMs, the AVAE model enables the integration of neural functional data with additional single-cell data modalities, such as

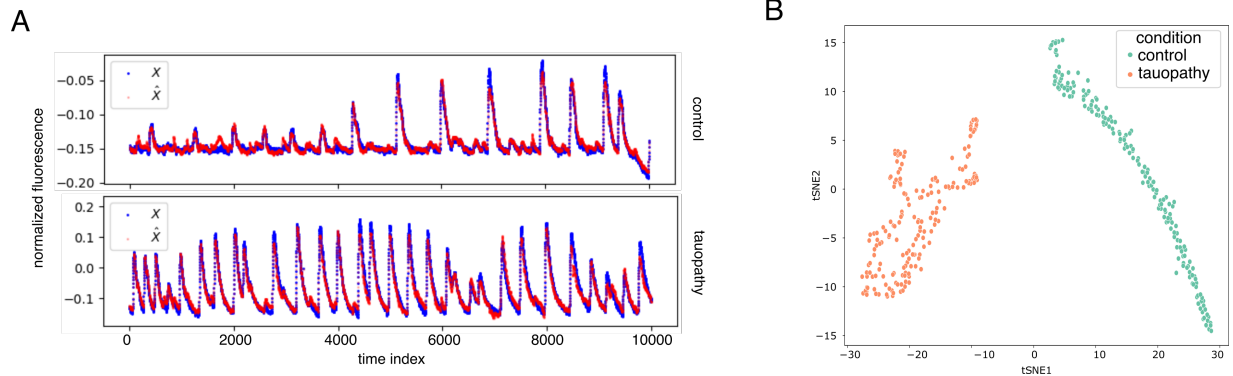


Figure 6: Reconstruction performance of the AVAE model ($D_1 = 128$, $D_2 = 8$) for the *in vitro* tauopathy model data. **A.** Representative examples of original X (blue) and reconstructed \hat{X} (red) signals in control (top) and diseased (bottom) neurons from the validation subset. **B.** t-SNE embedding of calcium recordings from an *in vitro* tauopathy model, showing control neurons (green) and diseased neurons (orange) from the validation subset. The latter exhibits a higher degree of heterogeneity than the former, probably due to connectivity differences.

scRNA-seq or spatial transcriptomics. This integration can enhance our understanding of the interplay between gene expression, connectivity, and functional dynamics. Furthermore, its ability to produce compact representations suggests applications in data compression, facilitating efficient storage and transmission of large-scale neuronal recordings. In the future, we aim to explore extensions of this model, incorporating dynamics (e.g., the evolution of the neuronal network along time) and isolating specific sources of variability.

5 Conclusions

We present an innovative single-neuron representation learning algorithm for calcium imaging data using an autoregressive variational autoencoder (AVAE). Through both simulated and real data, we demonstrate the AVAE’s capability to denoise signals and generate robust latent representations, outperforming traditional linear methods in clustering and reconstruction. By capturing underlying physical properties and connectivity patterns, the AVAE effectively differentiates between firing and connectivity types while providing insights into condition-specific heterogeneity. These results underscore the AVAE’s potential as a versatile tool for analyzing complex neural dynamics and lays out the foundations for future integration of multimodal datasets within computational neuroscience.

6 Data and code availability

The simulated and experimental data are available upon request. The code to generate the simulated data [28] and to train the AVAE model is publicly available at <https://github.com/angelopiga/neurons> and https://github.com/jordiabante/calcium_avae, respectively.

7 Ethical considerations

Neuronal cultures were prepared in accordance to the regulations of the Ethical Committee for Animal Experimentation of the University of Barcelona (approved ethical order B-RP-094/15–7125 of July 10th 2015) and the laws for animal experimentation of the Generalitat de Catalunya (Catalonia, Spain).

8 Competing interests

No competing interest is declared.

9 Author contributions statement

J.A. conceived the study; A.P., C.L., B.R., and J.A. conducted the experiments; B.R. and J.A. analyzed the results; and J.S., A.P., J.C., and J.A. wrote and reviewed the manuscript.

10 Acknowledgments

This study was supported by grants from the Ministerio de Ciencia e Innovación (PID2021-126961OB-I00, PID2022-137713NB-C22, PLEC2022-009401) funded by MCIU/AEI/10.13039/501100011033 and by ERDF/EU; Instituto de Salud Carlos III, Ministerio de Ciencia e Innovación and European Regional Development Fund (ERDF A way of making Europe) (Red de Terapias Avanzadas, RD21/0017/0020); European Union Horizon 2020 research and innovation program under Grant No. 964877 (project NEU-CHiP); European Union NextGeneration EU/PRTR; Generalitat de Catalunya (2021-SGR-01094 and 2021-SGR-00450); “la Caixa” Foundation under the grant agreements LCF/PR/HR19/52160007, LCF/PR/HR21-00622 and LCF/BQ/PI24/12040007; and Red Española de Supercomputación (RES) under project BCV-2024-2-0010.

References

- [1] Jason ND Kerr and Winfried Denk. Imaging in vivo: watching the brain in action. *Nature Reviews Neuroscience*, 9(3):195–205, 2008.
- [2] Jordi Soriano. Neuronal cultures: Exploring biophysics, complex systems, and medicine in a dish. *Biophysica*, 3(1):181–202, 2023.
- [3] Hideaki Yamamoto, Satoshi Moriya, Katsuya Ide, Takeshi Hayakawa, Hisanao Akima, Shigeo Sato, Shigeru Kubota, Takashi Tanii, Michio Niwano, Sara Teller, et al. Impact of modular organization on dynamical richness in cortical networks. *Science advances*, 4(11):eaau4914, 2018.
- [4] Marc Montalà-Flaquer, Clara F. López-León, Daniel Tornero, Akke Mats Houben, Tanguy Fardet, Pascal Monceau, Samuel Bottani, and Jordi Soriano. Rich dynamics and functional organization on topographically designed neuronal networks in vitro. *iScience*, 25(12):105680, 2022.
- [5] S. Fernández-García, J. G. Orlandi, G. A. García-Díaz Barriga, M. J. Rodríguez, M. Masana, J. Soriano, and J. Alberch. Deficits in coordinated neuronal activity and network topology are striatal hallmarks in huntington’s disease. *BMC Biology*, 18:1–16, 2020.
- [6] Andrea Comella-Bolla, Javier G. Orlandi, Andrés Miguez, Marco Straccia, María García-Bravo, Georgina Bombau, Mireia Galofré, Phil Sanders, Jordi Carrere, José Carlos Segovia, Joan Blasi, Nicholas D. Allen, Jordi Alberch, Jordi Soriano, and Josep M. Canals. Human Pluripotent Stem Cell-Derived Neurons Are Functionally Mature In Vitro and Integrate into the Mouse Striatum Following Transplantation. *Molecular Neurobiology*, 57(6):2766–2798, jun 2020.
- [7] G. Carola, D. Malagarriga, C. Calatayud, M. Pons-Espinal, L. Blasco-Agell, Y. Richaud-Patin, I. Fernandez-Carasa, V. Baruffi, S. Beltramone, E. Molina, P. Dell’Era, J. J. Toledo-Aral, E. Tolosa, A. R. Muotri, J. Garcia Ojalvo, J. Soriano, A. Raya, and A. Consiglio. Parkinson’s disease patient-specific neuronal networks carrying the LRRK2 G2019S mutation unveil early functional alterations that predate neurodegeneration. *npj Parkinson’s Disease*, 7(1):1–14, 2021.
- [8] Misha B. Ahrens, Michael B. Orger, Drew N. Robson, Jennifer M. Li, and Philipp J. Keller. Whole-brain functional imaging at cellular resolution using light-sheet microscopy. *Nature Methods* 2013 10:5, 10:413–420, 3 2013.
- [9] Tsai Wen Chen, Trevor J. Wardill, Yi Sun, Stefan R. Pulver, Sabine L. Renninger, Amy Baohan, Eric R. Schreiter, Rex A. Kerr, Michael B. Orger, Vivek Jayaraman, Loren L. Looger, Karel Svoboda, and Douglas S. Kim. Ultrasensitive fluorescent proteins for imaging neuronal activity. *Nature* 2013 499:7458, 499:295–300, 7 2013.
- [10] Estefanía Estévez-Priego, Martina Moreno-Fina, Emanuela Monni, Zaal Kokaia, Jordi Soriano, and Daniel Tornero. Long-term calcium imaging reveals functional development in hipsc-derived cultures comparable to human but not rat primary cultures. *Stem Cell Reports*, 18:1–15, 2023.
- [11] Chethan Pandarinath, Daniel J O’Shea, Jasmine Collins, Rafal Jozefowicz, Sergey D Stavisky, Jonathan C Kao, Eric M Trautmann, Matthew T Kaufman, Stephen I Ryu, Leigh R Hochberg, Jaimie M Henderson, Krishna V Shenoy, L F Abbott, and David Sussillo. Inferring single-trial neural population dynamics using sequential auto-encoders. *Nature Methods*, 15:805–815, 10 2018.
- [12] Ding Zhou and Xue-Xin Wei. Learning identifiable and interpretable latent models of high-dimensional neural activity using pi-vae. In *NeurIPS*, 2020.
- [13] Luke Y Prince, Shahab Bakhtiari, Colleen J Gillon, and Blake A Richards. Parallel inference of hierarchical latent dynamics in two-photon calcium imaging of neuronal populations. *bioRxiv*, 2021.
- [14] Felix Pei, Joel Ye, David Zoltowski, Anqi Wu, Raed H Chowdhury, Hansem Sohn, Joseph E O’doherly, Krishna V Shenoy, Matthew T Kaufman, Mark Churchland, Mehrdad Jazayeri, Lee E Miller, Jonathan Pillow, Il Memming

- Park, Eva L Dyer, and Chethan Pandarinath. Neural latents benchmark '21: Evaluating latent variable models of neural population activity. In *NeurIPS*, 2021.
- [15] Steffen Schneider, Jin Hwa Lee, and Mackenzie Weygandt Mathis. Learnable latent embeddings for joint behavioural and neural analysis. *Nature*, 617:360–368, 5 2023.
- [16] Mehrdad Jazayeri and Srdjan Ostojic. Interpreting neural computations by examining intrinsic and embedding dimensionality of neural activity. *Current opinion in neurobiology*, 70:113–120, 2021.
- [17] Joshua T Vogelstein, Brendon O Watson, Adam M Packer, Rafael Yuste, Bruno Jedynek, and Liam Paninski. Spike inference from calcium imaging using sequential monte carlo methods. *Biophysical journal*, 97:636–655, 2009.
- [18] Joshua T Vogelstein, Adam M Packer, Timothy A Machado, Tanya Sippy, Baktash Babadi, Rafael Yuste, and Liam Paninski. Fast nonnegative deconvolution for spike train inference from population calcium imaging. *Journal of neurophysiology*, 104:3691–3704, 2010.
- [19] Eftychios A Pnevmatikakis, Josh Merel, Ari Pakman, and Liam Paninski. Bayesian spike inference from calcium imaging data. In *2013 Asilomar Conference on Signals, Systems and Computers*, pages 349–353. IEEE, 2013.
- [20] Thomas Deneux, Attila Kaszas, Gergely Szalay, Gergely Katona, Tamás Lakner, Amiram Grinvald, Balázs Rózsa, and Ivo Vanzetta. Accurate spike estimation from noisy calcium signals for ultrafast three-dimensional imaging of large neuronal populations in vivo. *Nature communications*, 7:12190, 2016.
- [21] Eftychios A Pnevmatikakis, Daniel Soudry, Yuanjun Gao, Timothy A Machado, Josh Merel, David Pfau, Thomas Reardon, Yu Mu, Clay Lacefield, Weijian Yang, et al. Simultaneous denoising, deconvolution, and demixing of calcium imaging data. *Neuron*, 89(2):285–299, 2016.
- [22] Johannes Friedrich, Pengcheng Zhou, and Liam Paninski. Fast online deconvolution of calcium imaging data. *PLoS computational biology*, 13:e1005423, 2017.
- [23] Artur Speiser, Jinyao Yan, Evan W Archer, Lars Buesing, Srinivas C Turaga, and Jakob H Macke. Fast amortized inference of neural activity from calcium imaging data with variational autoencoders. *Advances in neural information processing systems*, 30, 2017.
- [24] Lucas Theis, Philipp Berens, Emmanouil Froudarakis, Jacob Reimer, Miroslav Román Rosón, Tom Baden, Thomas Euler, Andreas S Tolias, and Matthias Bethge. Benchmarking spike rate inference in population calcium imaging. *Neuron*, 90:471–482, 2016.
- [25] Kevin P Murphy. *Probabilistic machine learning: Advanced topics*. MIT press, 2023.
- [26] Diederik P Kingma and Max Welling. Auto-encoding variational bayes. *arXiv preprint arXiv:1312.6114*, 2013.
- [27] Javier G Orlandi, Jordi Soriano, Enrique Alvarez-Lacalle, Sara Teller, and Jaume Casademunt. Noise focusing and the emergence of coherent activity in neuronal cultures. *Nature Physics*, 9(9):582–590, 2013.
- [28] Akke Mats Houben, Jordi Garcia-Ojalvo, and Jordi Soriano. Role of connectivity anisotropies in the dynamics of cultured neuronal networks. *arXiv preprint arXiv:2501.04427*, 2025.
- [29] Eugene M Izhikevich. Simple model of spiking neurons. *IEEE Transactions on neural networks*, 14(6):1569–1572, 2003.
- [30] Enrique Alvarez-Lacalle and Elisha Moses. Slow and fast pulses in 1-D cultures of excitatory neurons. *Journal of computational neuroscience*, 26:475–493, 2009.
- [31] Nyantsz Wu, Walter K Nishioka, Noël C Derecki, and Michael P Maher. High-throughput-compatible assays using a genetically-encoded calcium indicator. *Scientific Reports*, 9(1):12692, 2019.
- [32] Yipeng Wang and Eckhard Mandelkow. Tau in physiology and pathology. *Nature reviews neuroscience*, 17(1):22–35, 2016.
- [33] Jürgen Götz, Glenda Halliday, and Rebecca M Nisbet. Molecular pathogenesis of the tauopathies. *Annual Review of Pathology: Mechanisms of Disease*, 14(1):239–261, 2019.
- [34] Javier G Orlandi, Sara Fernández-García, Andrea Comella-Bolla, Mercè Masana, Gerardo García-Díaz Barriga, Mohammad Yaghoubi, Alexander Kipp, Josep M Canals, Michael A Colicos, Jörn Davidsen, et al. Netcal: an interactive platform for large-scale, network and population dynamics analysis of calcium imaging recordings. *Neuroscience*, 2017.
- [35] Martin Ester, Hans-Peter Kriegel, Jörg Sander, Xiaowei Xu, et al. A density-based algorithm for discovering clusters in large spatial databases with noise. In *kdd*, volume 96, pages 226–231, 1996.
- [36] Laurens Van der Maaten and Geoffrey Hinton. Visualizing data using t-SNE. *Journal of machine learning research*, 9(11), 2008.

- [37] Sara Teller, Islam Bogachan Tahirbegi, Mònica Mir, Josep Samitier, and Jordi Soriano. Magnetite-amyloid- β deteriorates activity and functional organization in an in vitro model for alzheimer's disease. *Scientific Reports*, 5(1):17261, 2015.